Aerodynamic Performance of an Aircraft Equipped with Horizontal Tail-Mounted Propellers

van Arnhem, Nando; de Vries, Reynard; Vos, Roelof; Veldhuis, Leo

DOI
10.2514/6.2019-3036

Publication date
2019

Document Version
Final published version

Published in
AIAA Aviation 2019 Forum

AIAA AVIATION Forum
17-21 June 2019, Dallas, Texas
AIAA Aviation 2019 Forum

10.2514/6.2019-3036

Aerodynamic Performance of an Aircraft Equipped with Horizontal Tail-Mounted Propellers

Nando van Arnhem*, Reynard de Vries†, Roelof Vos‡, and Leo L. M. Veldhuis§
Delft University of Technology, Delft, 2629 HS, The Netherlands

This paper presents an experimental and numerical study of the aerodynamic interaction between horizontal tail-mounted propellers and the airframe. A representative aircraft model was installed in a low-speed wind-tunnel and measurements were taken with an external balance to determine the effect of propeller installation on integral forces and moments. Total pressure measurements were performed downstream of the model for qualitative analysis of the propeller–airframe interaction. The experimental data were complemented by full blade CFD analyses, which correlate excellently to the experimental data. Balance measurements indicate that the propeller installation results in an offset and a change in the slope of the pitching moment curve over the complete range of angles of attack. The extent to which the propellers contribute to the longitudinal control and stability was shown to be dependent on the angle of attack of the aircraft and the rotation direction of the propellers. The flowfield and computed propeller loads show that an inboard-up rotating propeller results in a neutral contribution to longitudinal stability towards higher angles of attack, while an outboard-up rotation enhances the stability for all positive angles of attack. The non-uniform inflow to the propeller induced by the airframe leads to a lateral shift of the thrust which influences the trim condition.

Nomenclature

$\mathcal{AR}$ = aspect ratio
b = span [m]
$c, \bar{c}$ = chord, mean aerodynamic chord [m]
C_D = drag coefficient, $\frac{D}{q_\infty S_w}$
C_L = lift coefficient, $\frac{L}{q_\infty S_w}$
C_m = pitching moment coefficient, $\frac{m}{q_\infty S_w \bar{c}}$
C_n = yawing moment coefficient, $\frac{n}{q_\infty S_w \bar{c}}$
C_N = normal-force coefficient, $\frac{N}{\rho_\infty n^2 d_p^4}$
C_{p_t} = total pressure coefficient, $\frac{p_t - p_{t\infty}}{q_\infty} + 1$
C_T = propeller thrust coefficient, $\frac{T}{\rho_\infty n^2 d_p^4}$
d = diameter [m]
D = drag [N]
J = propeller advance ratio, $\frac{V_\infty}{n d_p}$
l = length [m]
L = lift [N]
M = pitching moment [Nm]
n = rotational speed [s^{-1}], yawing moment [Nm]
N = normal force [N]
p = pressure [Pa]
P = power [W]
q = dynamic pressure [Pa]
Q = Propeller torque [Nm]
Q_c = propeller torque coefficient
r = radial coordinate [m]
R = radius [m]
S = area [m^2]
T = propeller thrust [N]
T_c = thrust coefficient, $\frac{T}{\pi/4 q_\infty d_p^2}$
V = velocity [ms^{-1}]
x, y, z = Cartesian coordinates [m]
α, β = angle of attack, angle of sideslip [deg]
δ = deflection [deg]
η = propulsive efficiency, $\frac{TV_\infty}{P}$
ρ = density [$kg \cdot m^{-3}$]

Subscripts

∞ = freestream quantity
e = elevator
f = flap
h = horizontal tail
p = propeller
s = slipstream
v = vertical tail
w = wing

Superscripts

’ = Local quantity

*Ph.D. Candidate, Flight Performance and Propulsion Section, Faculty of Aerospace Engineering, N.vanArnhem@tudelft.nl; AIAA member.
†Ph.D. Candidate, Flight Performance and Propulsion Section, Faculty of Aerospace Engineering, AIAA member.
‡Assistant Professor, Flight Performance and Propulsion Section, Faculty of Aerospace Engineering; AIAA Associate Fellow .
§Full Professor, Flight Performance and Propulsion Section, Faculty of Aerospace Engineering; AIAA member.

I. Introduction

The inherently high propulsive efficiency of propellers makes them an attractive means of propulsion for regional aircraft flying up to high-subsonic speed. A drawback of open-rotors, in particular for relatively high flight Mach numbers, is the cabin noise, driven by both airborne noise, as well as structure-borne noise. For this reason, a potential alternative to the wing-mounted propeller configuration are aft-mounted propellers, already proposed in the 1980's [1–3] of which an example is sketched in Fig. 1. A passenger aircraft featuring horizontal tailplane mounted propeller configuration is currently studied in the Clean-Sky European research project IRON (see Refs. [4, 5]) in which the technical disciplines of performance, safety, cost, stability and aerodynamic interaction are addressed. Such an aft-mounted layout may also be used for distributed propulsion systems where part of the propulsive power is placed near the tail of the aircraft, such as proposed in Ref. [6].

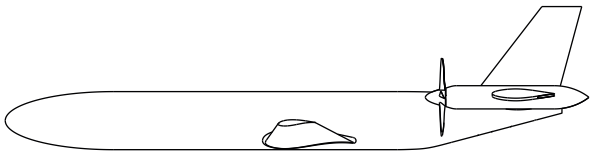

Fig. 1 Example of a tail-mounted propeller configuration.

However, such arrangement also brings challenges in terms of design, performance and operation. For example, as discussed in Refs. [4, 7], the inherently aft located center of gravity and the corresponding large range of center of gravity locations compared to wing-mounted propeller configurations, requires a careful analysis of the tail sizing, trim condition, and its associated induced losses. Furthermore, complex aerodynamic interactions between wing, propeller and stabilizing surfaces affect the stability and performance characteristics of the aircraft. It was found from initial studies [8, 9] that the overall longitudinal and lateral stability is not adversely affected by the propeller installation, attributed to a more effective horizontal tailplane and the stabilizing contributions of the propeller normal force [10, 11]. Changes due to the propeller installation of the integral forces and moments on a full aircraft geometry are presented in Applin and Coe [8] through an experimental campaign. An elaborate comparison study on the impact of such configuration on the performance, cost and design of a high subsonic passenger aircraft is discussed in Goldsmith [2]. In that study, the focus was on the comparison of overall performance of the tail-mounted propeller configuration rather than on the stability and control characteristics of the aircraft and aerodynamic interactions were not discussed in detail. The most detailed experimental campaign on such configuration is presented in Ridder [9], where inflow fields to the propeller were analyzed and integral force measurements were performed. However, a detailed study of the flow field and the decomposition of forces and moments on the different aerodynamic surfaces to explain the interaction phenomena were not presented. A more detailed breakdown of the relevant interaction phenomena of the airframe–propeller interaction is required to understand how the aerodynamic characteristics are altered for such an unconventional configuration.

Several studies on wing-mounted and wing-tip mounted propellers show a clear dependency on the induced drag, and therefore effective aspect ratio, due to the interaction of the propeller vortex system with the vortex system of the lifting surface [12–14]. Instead of tip-mounted propellers on the tailplane, more integrated designs are proposed [2] with the nacelle embedded in the horizontal tailplane. In those configurations, the close proximity of the propeller tip-vortex with the vortex stemming from the tailplane leads to an interaction which is likely to affect the tailplane effectiveness, and therefore the spanwise location of the propeller on the tailplane is likely to influence the stabilizing contribution of the propeller. The propeller forces are also affected by the installation due to the non-uniformity of the inflow introduced by the airframe, which constitutes a viscous and inviscid contribution, leading to unsteady loads on the blades. Subsequently, the propeller in-plane and out-of-plane forces affect the aircraft performance, trim and stability characteristics. Additionally, the non-uniformity of the inflow is propagated to the stabilizing surfaces as the slipstream is no longer axisymmetric [15].

The objective in this paper is to study the fundamental interactions of propellers mounted on a tailplane through experimental and numerical analyses, to identify the relevant interaction phenomena and determine how they affect the aircraft's stability and control. A full aircraft model is used to assess the aerodynamic interaction phenomena on both component and aircraft level. The experimental analysis allows for the assessment of a large range of operating conditions, where the time-average effect of the propeller installation on aircraft level is determined. The numerical analyses complement the experimental results for a limited number of cases to obtain the load distributions on the

tailplane, the propeller loading and to provide insight in the dominant interaction phenomena. Finally, measured and computed flowfield data provide a qualitative overview of the relevant interactions. The understanding of these aerodynamic interactions and identifying the driving parameters which affect the aerodynamic performance on aircraft level, will contribute to design choices and to the formulation of strategies to mitigate observed adverse effects.

II. Experimental Setup

A. Wind-Tunnel Model

The aircraft model that is used in this study has a representative geometry for a tail-mounted propeller configuration and the geometry is based on Refs. [2, 4, 8]. The wing has no sweep, a linear washout of 2 deg, an aspect ratio of 8.46 and a taper ratio of 0.40. To simulate an increased downwash to the tailplane, high-lift configurations were considered by deploying Junkers flaps, which were removed for the measurements on the clean configuration. Figure 2 shows all the relevant dimensions of the model and a cross section of the windtunnel.

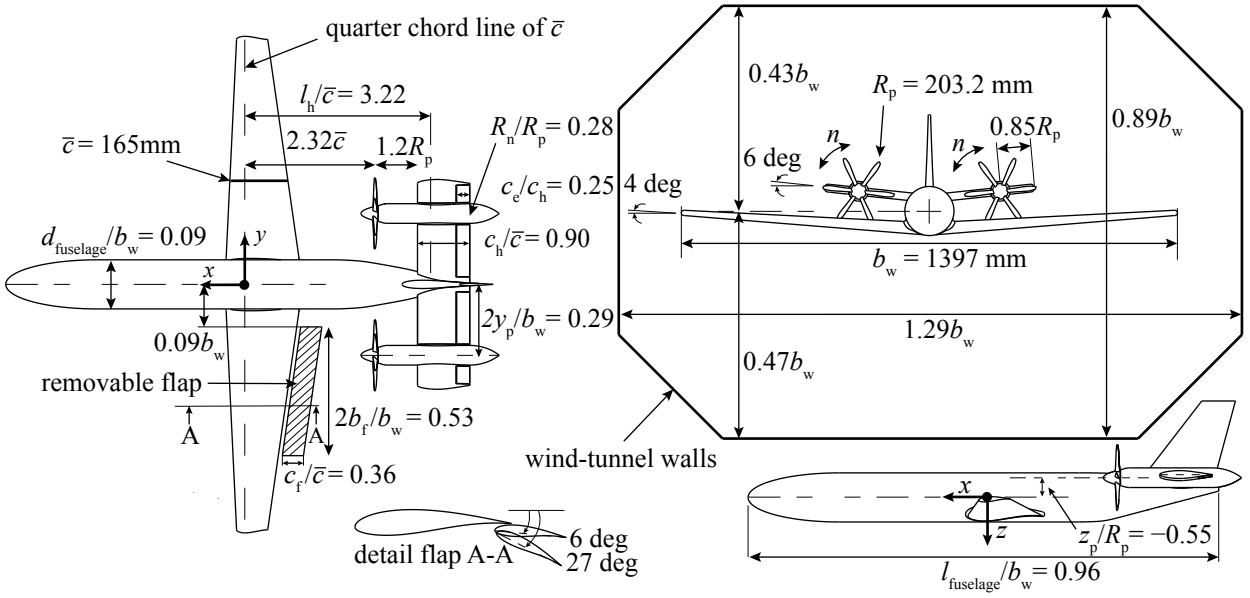

Fig. 2 Technical drawing of the aircraft model and wind-tunnel test section.

An overview of the geometrical properties of this aircraft are presented in Table 1. The tail volume coefficients, the propeller location and diameter are based on Refs. [2, 4, 8]. The propeller rotation axis is aligned with the fuselage centerline and its z-location results in a tail dihedral angle of 6 deg. The nacelle is mounted at 69% of the horizontal tail semi-span and is integrated with the horizontal tail. Both inboard and outboard parts of the horizontal tail are equipped with elevators with a chord ratio of 25%. The tip of the symmetric horizontal tail is rounded and extends up to $0.85R_p$ from the propeller rotation axis to reduce pressure fluctuation due to the impingement of the vortex core on the tailplane [16]. The distance between the propeller rotation plane and the leading edge of the tailplane is selected as $1.2R$, based on findings of Sinnige et al. [16].

To avoid laminar separation and for comparison with the fully turbulent CFD RANS simulations, transition strips of 2.5 mm width with carborundum particles with an average size of 150 μm were applied on the fuselage, wing, nacelle and tail surfaces, as indicated in Fig. 3. On the tail surfaces and wing pressure side the strips were applied at 10% of the chord, while on the wing suction side a strip was applied at 5% chord. Transition was checked for the considered range of operating conditions. The model was manufactured with a surface roughness of less than 0.4 μm and surface irregularities (e.g. countersunk holes) were filled with plasticine.

The model was equipped with two six-bladed steel propellers which are 1:2 scaled versions of the propeller used in Li et al. [17] with a slightly modified trailing edge to maintain a minimum trailing edge thickness of 0.2 mm. The propellers are driven by two water-cooled electric motors. In Ref. [18] the measured performance data for the isolated

Table 1 Overview of dimensions of aerodynamic surfaces of the aircraft model. The vertical tail is defined up to the curved local fuselage centerline.

	Wing w/o flap	Flap	Horizontal tail	Vertical tail
Area	0.2163 m^2	$\frac{2S_f}{S_w} = 0.19$	$\frac{S_h}{S_w} = 0.37$	$\frac{S_v}{S_w} = 0.18$
Airfoil	DU 96-150	DU 96-150	NACA 64_2A015	NACA 0015
Root incidence, washout angle	0 deg, 2 deg	-, 0 deg	0 deg, 0 deg	0 deg, 0 deg
Aspect ratio	8.46	6.10	2.85	1.50
Taper ratio	0.40	1.00	1.00	0.41
Volume coefficient	-	-	1.14	0.54
Control surface area	-	-	$0.17S_h$	$0.28S_v$

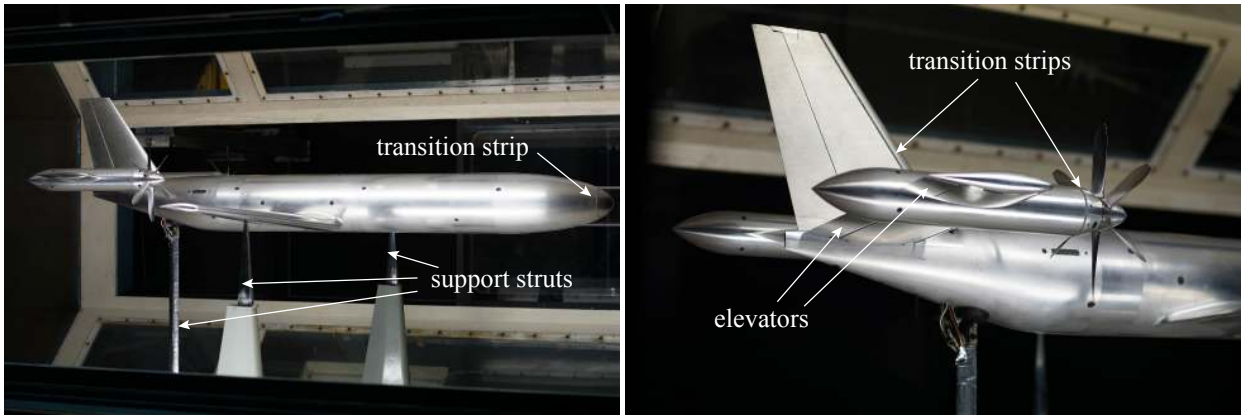

(a) Model with tail-mounted propellers

(b) Horizontal tail with split elevators

Fig. 3 Horizontal tail mounted propeller configuration installed in the Low Turbulence Tunnel at Delft University of Technology.

propeller at zero incidence is presented. Compared to full-scale, high speed propellers with a large number of blades and high tip Mach number, the typical maximal thrust coefficients of an experimental setup are inherently lower. In e.g. Refs. [18, 19] it was shown that small propellers used in typical wind-tunnel setups exhibit strong Reynolds number effects, which further reduce the maximum achievable thrust coefficients. To obtain a similar slipstream shape, a similar ratio of q_s/q_∞ and similar propeller forces relative to the airframe, the values of C_T, C_Q, J and at the same time, T_C and Q_C should ideally match with full-scale conditions. This is illustrated by Fig. 4, which indicates the operating conditions of a scaled propeller relative to representative full-scale propeller conditions. A rather large blade pitch angle of 45±0.05 deg at 70% radius was selected to approach the force coefficients in full-scale condition. Although this study is on a conceptual model, it is noted that the conditions presented in this paper aim to simulate cruise and landing conditions, rather than take-off and climb conditions. For the latter, propellers with more blades, a high Reynolds number and more powerful motors would be required to achieve a disk loading comparable to full-scale condition.

B. Wind-Tunnel Facility, Measurement Techniques and Test Conditions

The experimental campaign was performed at the Low-Turbulence Tunnel (LTT) at Delft University of Technology, a closed-return low-speed wind-tunnel. The aircraft model was suspended by a three-point support system (Fig. 3) connected to a six-component external balance and allows for variation of both angle of attack and side-slip. The model was installed in an octagonal testsection with its dimensions indicated in Fig. 2. The maximum area ratio of the model and supports is approximately 3%. No wind-tunnel corrections are applied to the current results. Throughout the experiment, the propeller advance ratio was set based on V_∞. This means that the effective advance ratio in the installed

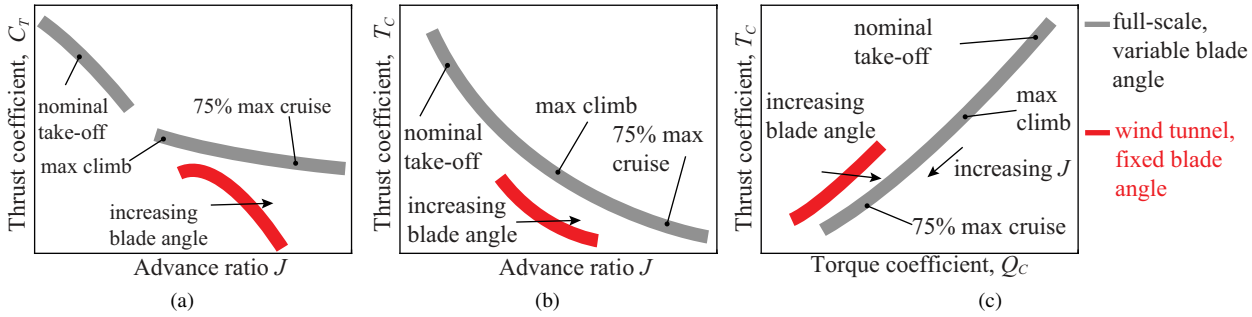

Fig. 4 Illustration of typical operating conditions for full-scale vs. wind-tunnel scale propellers. The red curve represents approximately the operating conditions in this paper.

case is slightly higher due to the presence of the windtunnel walls.

An acquisition time of 20 seconds was selected to average the measured force data. For the considered range in aerodynamic forces, the balance has an uncertainty of 0.002 N to 0.01 N, depending on the force component. Two times these values are included in the error-bars of the respective force measurements. These error-bars also include the spread in data of repeat measurements due to for example hysteresis or variations in operating conditions. It was found that the blade-pitch angle could be set with an accuracy of ±0.05 deg. The associated uncertainty in propeller thrust was determined using the numerical model of the isolated propeller [18] and is included in the error-bars for C_D and C_X. Balance measurements were corrected by subtracting the aerodynamic forces of the support struts, which were measured separately.

A DTC-Initium pressure scanner was used to determine the total pressure and static pressure far upstream of the model, which combined with a calibration of the test section results in the dynamic pressure of the freestream. A measurement uncertainty of ±4Pa on this dynamic pressure is included in the error-bars of the force coefficients. For validation purposes and to illustrate the propeller-airframe interaction, total pressure measurements were taken using a wake rake connected to the same pressure scanner at a plane downstream of the model, perpendicular to the freestream flow. The resolution of this grid was 3mm in both y and z-direction. For the balance measurements, the wake rake was not installed to eliminate its upstream effect on the model. The pressures were averaged over 5 seconds of acquisition time.

A freestream velocity of 40 m/s ($Re_{\bar{c}} = 4.54 \cdot 10^5$) was selected based on the electric motor operational limits. At this velocity, the turbulence level was below 0.1%. Both propeller-off and propeller-on measurements were performed, where the advance ratio was varied from $J = 2.3$ up to $J = 1.6$ by varying the rotational speed to achieve thrust coefficients between $T_C = 0.01$ and $T_C = 0.28$. The accuracy of the rotational speed was 0.01 Hz, with maximum fluctuations up to 0.1 Hz around the mean value were observed. Both inboard-up (IU), outboard-up (OU) and co-rotating (CO) configurations are considered to quantify the effect on longitudinal and lateral stability and trim. An angle of attack range of −5 to +14 deg was measured for all cases, while the side slip was varied over a range of −10 to +10 deg. The elevator was deflected up to 15 deg, and for high-lift conditions the flap was deflected by +6 deg and +27 deg.

III. Computational Setup and Validation

A. Computational Strategy

The numerical analyses are performed to quantify the aerodynamic interaction between the propeller and airframe on component level. This interaction is time dependent and is driven by both viscous and inviscid flow phenomena. To this end, a half model excluding support struts, shown in Fig. 5, is simulated by solving the RANS equations for compressible flow. The geometry is an accurate representation of the wind-tunnel model and contains the gaps around the elevators, while the gap between the spinner and nacelle, and the gaps associated to the rudder, are sealed for simplicity. The model is placed in a domain with the outer boundaries resembling the wind-tunnel walls. The relative location of the walls to the aircraft model is equal to the dimensions in Fig. 2. An angle of attack is simulated by rotating the model about the same axis as in the experimental setup. Tapering of the wind-tunnel walls to compensate

for the buoyancy effect introduced by the boundary layer formed on the wind-tunnel walls is not included in the numerical simulations. Instead, a domain is used without taper and the walls are modelled as slip walls. On the airframe components, which are modelled as no-slip walls, standard roughness is assumed. The pressure inlet and pressure outlet boundary conditions are placed far upstream and downstream of the model respectively, on which the flow direction is enforced to be normal to these boundaries. On the outlet boundary, the average pressure is specified to be equal to ambient conditions.

The unstructured volume mesh contains tetrahedral elements with refined grids in the proximity of the model. The domains containing the wing and the tailplane extend $2.5D$ downstream of propeller location. The propeller is placed in a rotating domain using the sliding mesh approach [20] by defining interfaces on each side. The grid of one propeller blade is copied to construct a full revolution to ensure an axisymmetric domain. Similarly to Ref. [18] a diverging rotating domain is chosen to maintain the propeller tip-vortex in this refined volume when an angle of attack is simulated to avoid excessive dissipation and diffusion of the tip-vortex which would occur in the coarser outer domain. Wall refinements are applied and an inflation layer of 25 layers with a growth rate of 1.20 is constructed on all no-slip walls. The first-layer thickness on each component was selected to comply with they requirement of the turbulence model for a $y^+ \leq 1$. The same propeller grid as presented in Ref. [18] was used. The same reference presents the accompanying discretization error and a comparison of the propeller slipstream for different mesh densities. The sizing of the adjacent domain to the rotating domain containing the horizontal tail is also based on Ref. [18]. The selected grid of the half model including propeller domain contained 60.5 million cells, while the grid of the propeller-off condition contained 51.8 million cells.

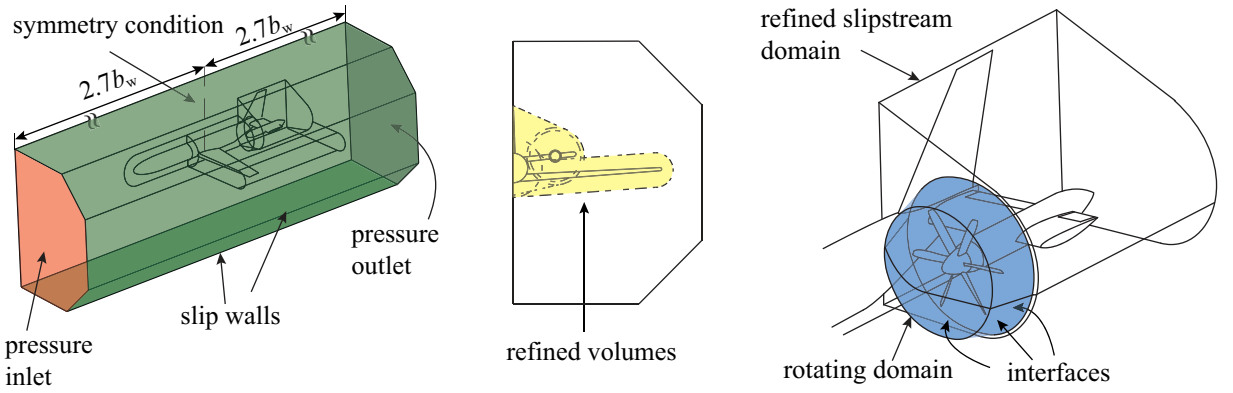

(a) Boundary conditions for CFD simulations. wind-tunnel domain extends further upstream and downstream than shown in sketch.

(b) Volume refinements in proximity of model.

(c) Detailed view of the rotating domain containing the propeller.

Fig. 5 Computational domain and boundary conditions used for the simulations. Dimensions of the cross section of the wind-tunnel test section correspond to values noted in Fig. 2.

ANSYS® Fluent Release 18.1 [20], an unstructured finite volume cell-centered solver, was used to perform the simulations. The flow was prescribed to be fully turbulent using the Spalart–Allmaras turbulence model with the strain/vorticity-based production equation, which has shown to compare well with experiments on problems with a similar range of Reynolds number and comparable aerodynamic interaction [21]. The inlet eddy-viscosity ratio of 0.21044 is based on recommendations by Spalart and Rumsey [22]. The simulations without propeller are steady, while the full-blade simulations are solved in a time-accurate manner, with a time step equivalent to 2 deg propeller rotation with 35 inner iterations. Second-order spatial and temporal discretizations are used, in line with e.g. Stokkermans et al. [21], with a coupled pressure-velocity scheme. Standard sea-level atmospheric conditions are assumed for the freestream flow. For the equation of state, the fluid is assumed to be an ideal gas with Sutherland's law using the three-coefficient method to predict the corresponding dynamic viscosity.

B. Validation of CFD Model

To gain confidence in the CFD simulations, the solutions on the selected grid are compared with experimental results. In particular, the inflow field to the propeller and the propeller-airframe interaction are important flow phenomena that are required to be captured by the CFD model. The total pressure field downstream of the model is therefore a relevant quantity to compare, as it encompasses the distribution of downwash and viscous drag for both wing and tail surfaces. It is noted that, compared to a five-hole probe, a wake-rake results in inaccuracies in the total pressure measurement in regions with large angles with respect to the probe, i.e. near vortex cores. This means that measured values in the shear layer of the slipstream are less accurate.

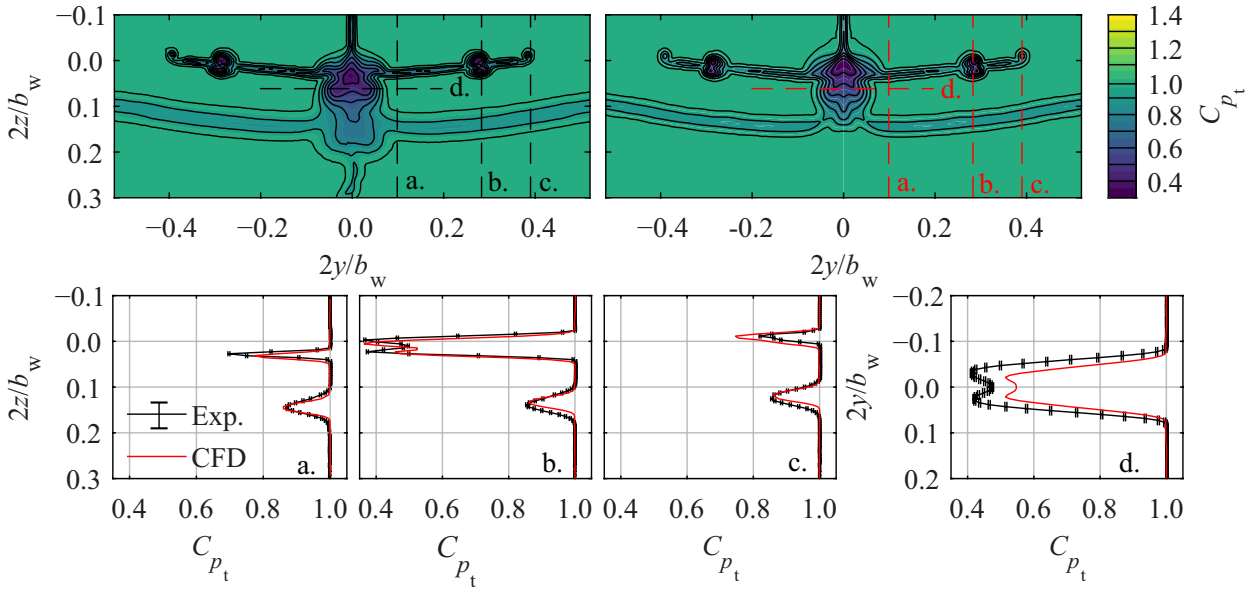

(a) Clean configuration, propeller off, α = 5 deg

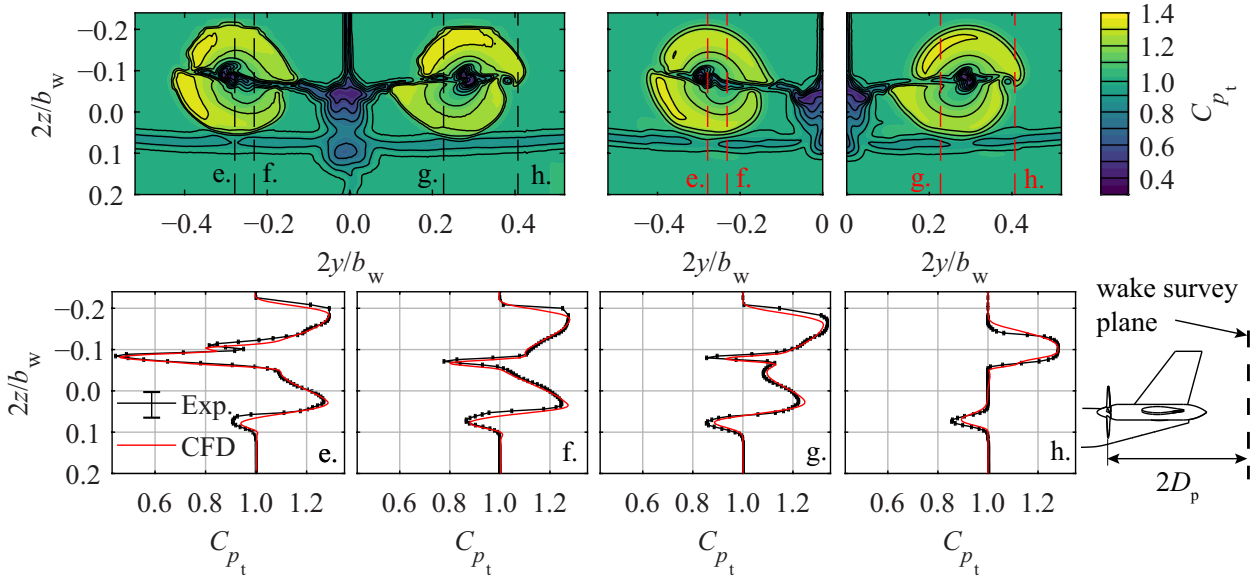

(b) Clean configuration, J=1.8, α = 0 deg. Time-accurate CFD results are time averaged over 60 deg of rotation (30 time steps).

Fig. 6 Measured total pressure coefficient in a wake survey plane of compared with CFD.

Figure 6a compares measured and computed the C_{p_t} fields at a plane two diameters downstream of the propeller with the model installed at an angle of attack of α = 5 deg . Qualitatively, all flow features observable in the experimental

data are also present in the CFD results. To compare quantitatively, the C_{p_t} is plotted along four survey lines, depicted in the same figure. Survey lines *a* through *c* show that the location of the wing wake is excellently predicted by the CFD on the inboard side, with a slight underprediction of the downwash on the outboard sections. While the minimum C_{p_t} almost coincides with the experimental result, the wake thickness in the CFD is slightly underpredicted. It is expected that this is associated with the applied transition strips on the model, which are relatively thick and therefore lead to a more rapid growth of the boundary layer. The deviation of the C_{p_t} of the tailplane wake (survey line *a*) is a combination of the underprediction of viscous drag and diffusion of the wake. However the corresponding z-location is predicted well, which indicates that the combination of local downwash produced by the wing and tailplane is captured. Also the prediction of the nacelle wake (survey line *b*) shows excellent agreement with experimental results, including the double peak originating from the merging of upper and lower boundary layer formed on the nacelle. The deviation of the reduced C_{p_t} in the vortex core (survey line *c*) is found to be due to a slightly more inboard location of the tip-vortex in the experiment. The largest deviation in the wake plane can be observed in the vicinity of the fuselage (survey line *d*), where the experiment clearly shows a larger momentum defect, although the particular shape from the merging of the boundary layer on each side is clearly present in the CFD result.

To compare the propeller-airframe aerodynamic interaction, the slipstream deformation and the magnitude of the C_{p_t} of the propeller-on configuration are shown in Fig. 6b. The time accurate CFD results are time averaged to compare with the measured C_{p_t}. Only for the co-rotating case experimental data is available, while only the inboard-up and outboard-up cases are simulated. It is noted that for the co-rotating case there is a sidewash as a result of the slipstream–tailplane interaction which is absent in the CFD simulations due to the symmetry condition. The slipstream location is slightly different and hence pressure data along the survey lines should be compared with care. The cropped contours on the upper side of the slipstream are an artefact of lower resolution of the wake rake data in the upper region of the plane. Qualitatively, all details of the measured flow field are also present in the CFD results, i.e. the shear of the slipstream, the non-axisymmetric loading of the propeller and the interaction of the propeller tip-vortex with tailplane tip-vortex. Quantitatively, the survey lines show excellent agreement as well, except for the regions near the edges of the propeller slipstream. It is found in e.g. Ref. [21], the large gradients in these shear layers are often quickly diffused downstream of the propeller in the numerical simulation, despite the fine grid in the slipstream domain. Therefore, also the interaction with the wing wake, which impinges the propeller tip, is less pronounced.

The underprediction of fuselage drag will primarily lead to an underprediction of C_{D_0}, but is not considered to be detrimental to the propeller–airframe interaction study. This is also observable in Fig. 7a and b which depict the integral force coefficients. The drag-curve shows that there is a clear offset with the experimental data, attributed to an underprediction of drag, particularly for the fuselage. The lift-curve shows that there is good agreement with the experimental data, although there is a slightly lower lift curve slope in the experiment, possibly due to the decambering-effect of the boundary layer at higher lift coefficients. It is noted that a typical cruise lift coefficient of 0.5 to 0.6 [4] is only attained at a relatively high angle of attack of $\alpha = 4$ deg.

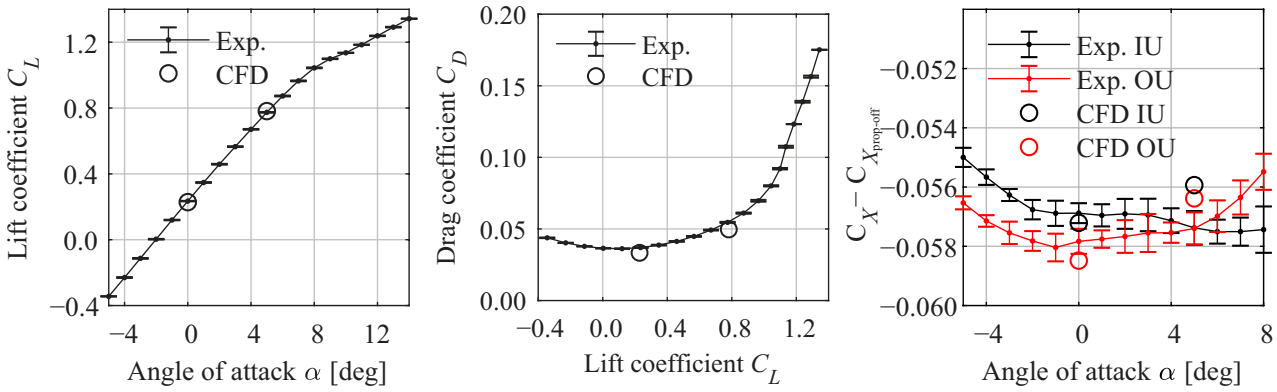

(a) Clean configuration, propeller-off (b) Clean configuration, propeller-off (c) Clean configuration, $T_C = 0.18$

Fig. 7 Measured force coefficients compared with CFD.

In terms of integral forces, the change in axial force coefficient due to the propeller installation, $\Delta C_X = C_{X_{\text{prop on}}} - C_{X_{\text{prop off}}}$, is plotted in Fig. 7c. The difference between inboard-up and outboard-up is primarily a difference in tailplane drag, as discussed in the next section. The figure shows that the deviation of ΔC_X between CFD and experiment is between 0.5 and 1.5% and falls nearly within the experimental error-bars for $\alpha = 0$ deg. It is concluded that the agreement of the CFD model with experiment for both the integral forces and flowfields for this scale is sufficiently accurate to predict the aerodynamic interactions and the associated trends.

IV. Results

In the following sections the findings of the experimental and numerical studies are presented in three subsections. Firstly, the overall effect of the propeller on the aircraft aerodynamic coefficients is presented in Section IV.A. The findings are supported by flowfield measurements. Secondly, the propeller installation effect on the directional stability and trim is discussed in Section IV.B. Finally, the change in propeller loading and its slipstream is discussed in Section IV.C.

A. Propeller Installation Effects on Longitudinal Stability, Trim and Control

1. Integral Forces and Moments

Prior to a breakdown of the propeller-airframe aerodynamic interaction, the effect of propeller installation on the integral aerodynamic coefficients is studied. Figure 8a shows the moment coefficient for the clean configuration and for two flap deflections with the quarter chord of the mean aerodynamic chord as reference point. The reader is reminded that the propeller forces are not measured for the installed condition and the T_C noted in the figures refers to the measured thrust of a *single* isolated propeller. The propeller installation results in a slightly more negative C_{m_α} and a small offset in moment curve. This offset is a combination of the nose down pitching moment due to the selected z-location of the propeller, a change in load on the horizontal tailplane and the propeller normal force contribution. The latter is a function of the wing downwash angle. Hence, the angle of attack at which there is no change in C_m, shifts with the deflection of the flaps. The more negative slope is the result of the propeller normal force gradient $C_{N_{p_\alpha}}$ and the altered C_{N_α} of the tailplane.

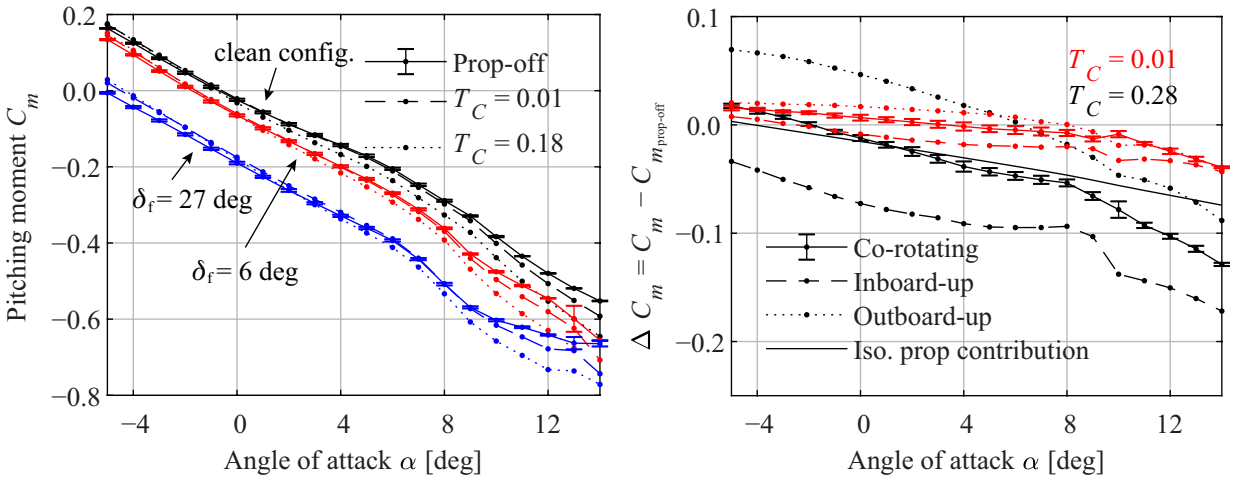

(a) Pitching moment coefficient for clean configuration and two flap settings with co-rotating propellers.

(b) Change in pitching moment coefficient for the clean configuration.

Fig. 8 Measured effect of the propeller installation on the pitching moment coefficient. Reference point is quarter chord of the wing mean aerodynamic chord. Error-bars only shown for a few cases to improve readability.

A better insight in the these changes due to the propeller installation can be gained by considering the change in moment coefficient, shown in Fig. 8b for the co-rotating, outboard-up and inboard-up configurations, for a low and medium thrust condition. As a reference, the contribution of the isolated propeller at $T_C = 0.18$ is also plotted which

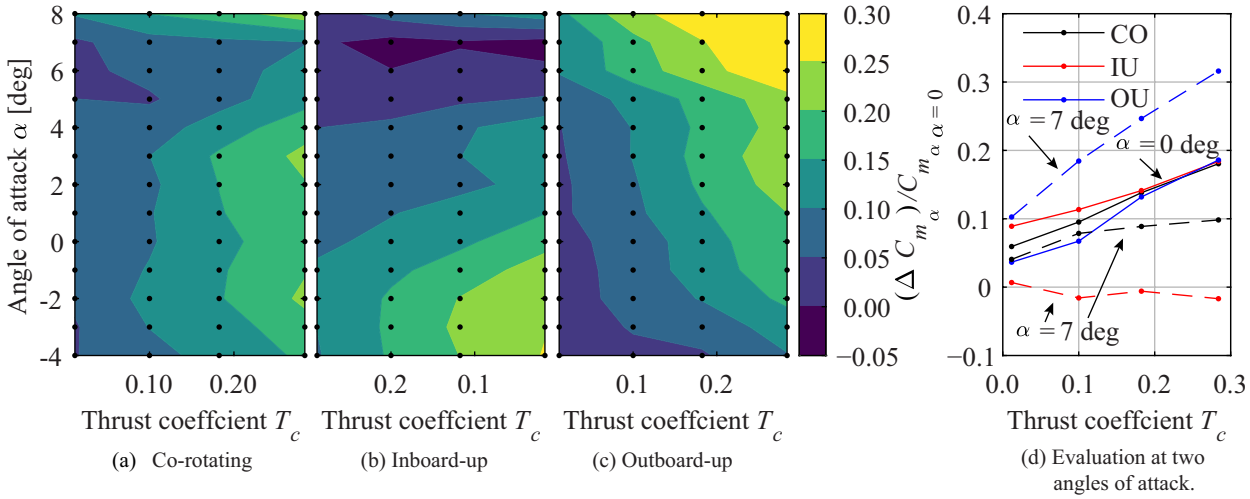

Fig. 9 Measured effect of the propeller installation on the C_{m_α} relative to propeller-off condition at zero angle of attack.

includes the thrust induced nose-down pitching moment and the predicted moment generated by the propeller normal force. The normal force is predicted using $C_{N_{\alpha_p}} = 0.58\ \text{rad}^{-1}$ computed by CFD analysis of the isolated propeller (not shown in this paper), and assuming $\alpha_p = \alpha - \alpha_i$ with $\alpha_i = C_L/(\pi \mathcal{A} e)$, with α_i independent of z-location and Oswald efficiency factor $e = 0.8$. A number of observations are made. Firstly, there is a clear offset in the moment curve, in particular for the inboard-up and outboard-up propeller rotation, due to the difference in swirl angle creating either a positive or negative normal force on the inboard part of the tailplane, also shown in Fig. 10a. It is interesting to note that the ΔC_m curve of the co-rotating case coincides with the average (not shown in the figure) between the IU and OU configurations, indicating that this asymmetry has negligible effect on the pitching moment behaviour over the full range of angle of attack. For both low and medium thrust condition, for the inboard-up case the gradient of ΔC_m becomes less negative up to $\alpha = 8$ deg, contrary to the outboard-up case, which becomes more stable up to $\alpha = 8$ deg. The figure also indicates that the propeller normal force and thrust induced pitching moment is a major contributor to the change in the moment curve.

A more complete assessment of the propeller installation on longitudinal stability can be made using Fig. 9, which shows the change in moment coefficient, $\Delta C_{m_\alpha} = C_{m_\alpha} - C_{m_{\alpha\,\text{prop-off}}}$, relative to the reference value $(C_{m_\alpha})_{\alpha=0}$. Therefore, a more positive value means enhanced longitudinal stability. The co-rotating case shows a rather monotonic behaviour; for all angles of attack the propeller positively contributes to longitudinal stability with higher T_C. The outboard-up case becomes more stable towards higher α and higher T_C. For the inboard-up case for each thrust setting, C_{m_α} becomes less negative towards higher angle of attack. For a given angle of attack up to $\alpha = 4$ deg, a higher T_C results in a more stable aircraft. However, around $\alpha = 6$ to 8 deg, counter-intuitively, a higher T_C does not result to a change in C_{m_α}, despite the on average higher dynamic pressure encountered by the tailplane and the normal force produced by the propeller. The most right subplot in Fig. 9 indicates that at $\alpha = 7$ deg there is even a slightly negative trend. At negative angles of attack, the inboard-up configuration follows the trend comparable to the outboard-up case at higher angle of attack. It is clear that the rotation direction of the propeller plays a key role on the longitudinal stability. For wing-tip mounted applications, an inboard-up propeller rotation results in an increase in effective aspect ratio as the induced losses of the propeller-wing combination are reduced [13]. However, in Fig. 9, the opposite is observed. Because the contribution of the propeller normal force for an isolated propeller is not dependent on rotational direction, the mechanism behind this is to be sought in the loads on the airframe.

2. Tailplane Effectiveness

The factors that determine the normal force gradient C_{N_α} of the tailplane, is a combination of both the vortex system from the propeller and tailplane, as well as the local propeller induced dynamic pressure and flow angle. The former is a highly three-dimensional interaction, while the last two factors can be interpreted as two-dimensional phenomenon. For insight in how the effectiveness of the tailplane is altered by the propeller installation, the tailplane load distribution is evaluated. Figure 10a shows the computed normal force distribution over the horizontal tailplane. In the propeller-off condition the wing downwash leads to a downforce on the tailplane. The propeller introduces the typical induced load distributions [14], with an increase or decrease in load depending on rotation direction of the swirl of the slipstream. At 0 deg angle of attack, the direction of the tailplane tip-vortex is clearly determined by the propeller rotation direction, noticeable by the load distribution towards the tailplane tip. The direction of the tailplane tip-vortex is opposite to the axial component of vorticity of the propeller tip-vortex, as shown in the isosurfaces of vorticity in Fig. 11a. For a positive angle of attack, these vortices are opposing for the outboard-up case, while they have the same sign in the inboard-up case, schematically shown in Fig. 11b. The sign of the axial component of these vortices partially determine the effective angle of attack to the tailplane. If the vortices are opposite in sign and in close proximity, their combined effect is a reduced downwash, and hence can be interpreted as an increase in aspect ratio. A measure for the induced losses is the in-plane kinetic energy, shown in Fig. 11c. Compared to propeller-off condition, the inboard-up case shows reduced in-plane losses in the inboard side of the tailplane, as a result of swirl recovery, while at $y'/R > 0$ the in-plane kinetic energy is spread out as a result of the propeller swirl and the induced field by the interaction of the two tip-vortices. At the same location, the in-plane kinetic energy is significantly lower for the outboard-up case, as the result of the counteracting vortices. Only a small region of high kinetic energy is observed as the tailplane and propeller tip-vortices are not exactly at the same location and their magnitude is not equal. A similar flowfield is also observed in Ref. [12]. It is therefore expected that the addition of the outboard part of the horizontal tail for the inboard-up propeller rotation results in a reduction of normal force gradient of the tailplane which is partially *opposing* the reduced induced losses for a wing-tip mounted configuration.

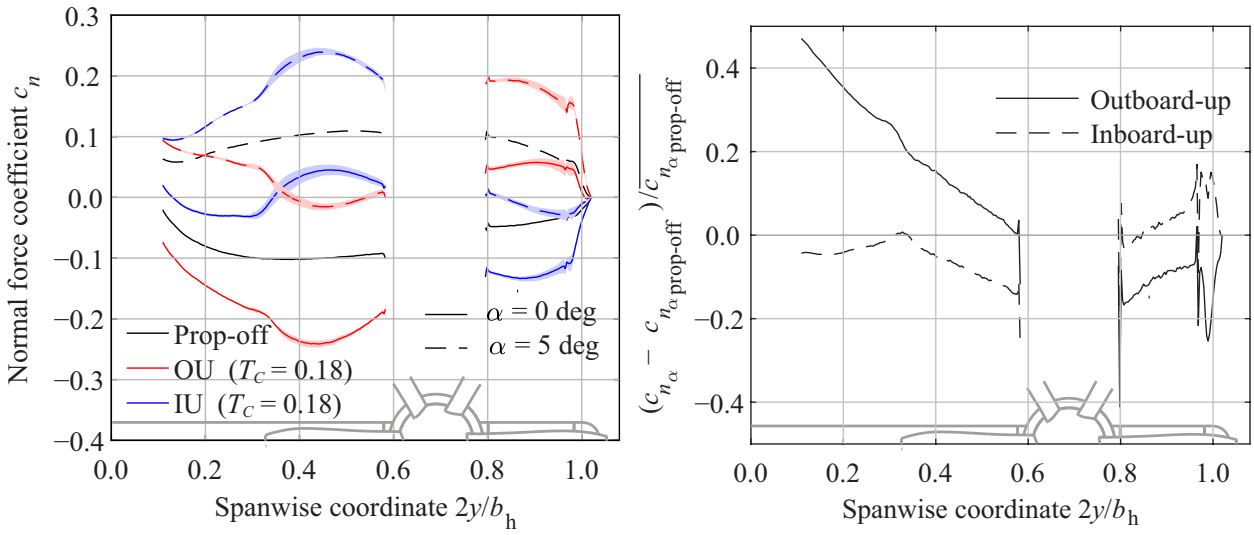

(a) Computed distribution of normal force coefficient of the tailplane. The shaded areas are the maximum fluctuations over a full propeller rotation.

(b) Computed change in local normal force gradient, computed over $\alpha = 0$ deg to $\alpha = 5$ deg, relative to the mean value of c_{n_α} in propeller-off conditions.

Fig. 10 Computed effect of propeller installation on the tailplane load distribution.

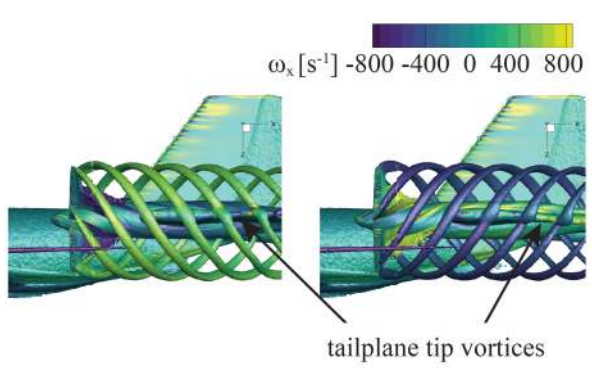

(a) Isosurface of vorticity magnitude at 800 s^{-1} for outboard up (left) and inboard-up configuration at zero angle of attack.

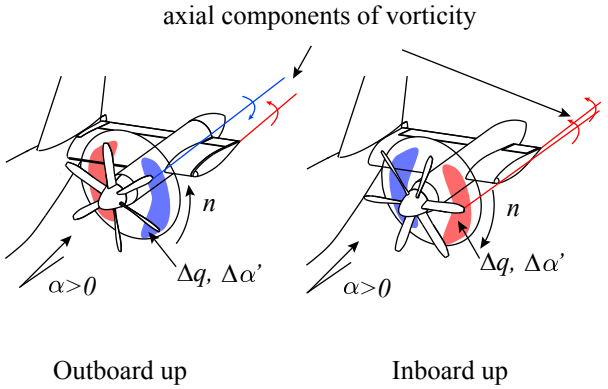

(b) Qualitative representation of change in dynamic pressure and direction of axial vorticity components between inboard-up and outboard-up rotation.

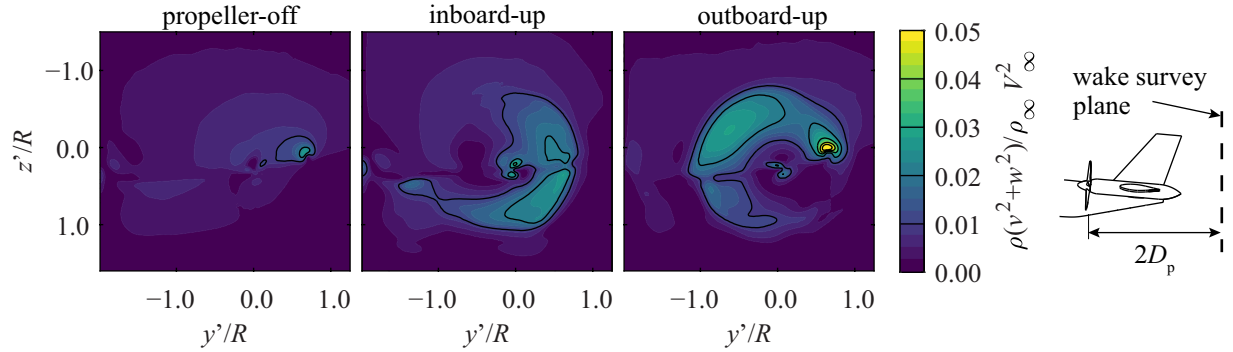

(c) Computed time-averaged in-plane kinetic energy relative to freestream kinetic energy at $\alpha = 5$ deg and $T_C = 0.18$.

Fig. 11 Quantitative and qualitative comparison of interaction between propeller-vortex system and tailplane tip-vortex.

The factors that also influence the *gradient* of the local normal force coefficient are the rates at which the dynamic pressure and local angle of attack change with airplane angle of attack. To understand the relative contributions of these two, the computed time-averaged flowfield between the propeller and horizontal tailplane is plotted in Fig. 12. As discussed in the next section, at $\alpha = 0$ deg the wing generates a downwash such that the thrust of the upgoing and downgoing blades increases and decrease, respectively. This leads to higher and lower total pressure coefficients, respectively. A vertical survey line on the inboard side of the tailplane clearly shows that at this location of the horizontal tail, the C_{p_t} increases by approximately 0.1, for an outboard-up rotation, while the local angle of attack induced by the propeller increases by approximately 1 deg when the aircraft angle of attack is increased from $\alpha = 0$ deg to $\alpha = 5$ deg. A reduction by approximately the same values are found for the inboard-up case. A 2D calculation (not shown in this paper) reveals that the *rate of change* of the induced angle of attack has a larger contribution than the dynamic pressure to the *rate of change* of the section lift coefficient. The combined effect of the vortex interaction and the local contribution of the slipstream leads to an altered distribution of c_{n_α}, depicted in Fig. 10b. The outboard-up case exhibits a higher c_{n_α} than the propeller-off case on down-going side and a lower c_{n_α} on the up-going side, in line with the preceding discussions, and extends beyond the edge of the propeller slipstream in the inboard part of the tailplane. The inboard-up case shows the opposite trend and curve indicates even a reduced effectiveness of the horizontal tailplane compared to propeller-off conditions.

The observed non-axisymmetry of the slipstream between propeller and tailplane in Fig. 12a is also traceable after it interacts with with the tailplane, shown in the measure flowfield in Fig. 13. The shear of the slipstream in the co-rotating arrangement is clearly visible in the C_{p_t} distribution, characterized as a positive velocity in y-direction on the upper side of the tailplane. For a wing-mounted configuration, this shear is also present and leads to a sidewash on the vertical tailplane and an accompanying yawing moment. However, for the rear-installation, the shear only starts at the leading edge of the horizontal tail and therefore the shear is primarily formed downstream of the vertical tail.

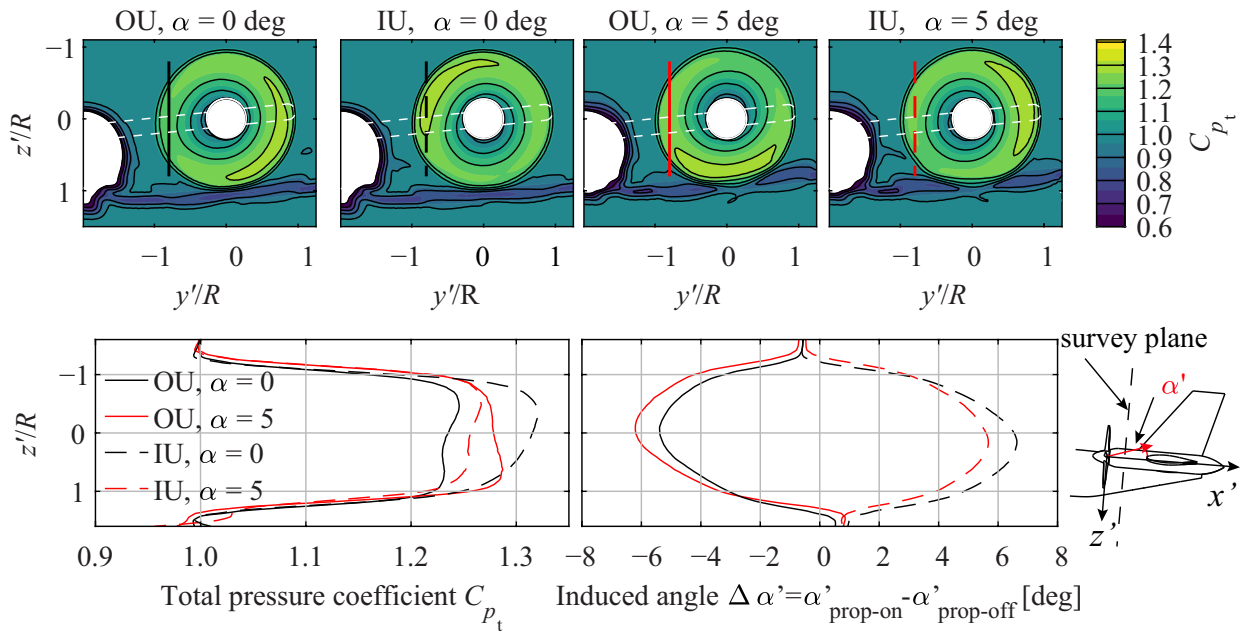

Fig. 12 Computed time-averaged flowfield between the propeller and horizontal tail for two angle of attack at $T_C = 0.18$.

At $\alpha = 10$ deg, in addition to a larger portion of the the wake that impinges the propeller, another non-uniformity is introduced. The two large areas of reduced total pressure are attributed to vortical flow from the wing-fuselage junction and from the fuselage, observed in oil-flow flow visualization and CFD analysis (not shown in this paper). In the installed configuration, part of this low axial momentum and swirling flow impinges the outer radii of the propeller. The swirl of this inflow is such that the downgoing blade of the outboard-up rotating propeller locally encounters a higher local angle of attack, leading to a local increase in blade loading, observable as higher C_{p_t}. It should be noted that this condition is highly dependent on the design of the wing-fuselage juction, which for the considered geometry is merely a fillet geometry.

In a typical high-lift condition, the flowfield near the propeller is characterized as a larger downwash and by the inboard flap edge vortex. The former results in a larger lateral shift of the thrust vector, clearly visible in the wake measurements in Fig. 13. The induced flowfield of the flap edge vortex also affects the deformation of the slipstream. As the propeller does not induce a swirl outside its slipstream [23], the location of the flap-edge vortex is almost unaltered compared to propeller-off conditions. Despite the large deformation of the slipstream, the trend of the moment curve of the high-lift configuration is comparable to the clean-configuration, as depicted in Fig. 8a.

From a design perspective, the change in the location of the neutral point is a relevant measure and is presented in Fig. 14a for the clean configuration. For all angles of attack, the neutral point is shifted aft for the co-rotating and outboard-up case, with a more rearward shift for the outboard-up case, while the neutral point at $T_C = 0.18$ and $\alpha = 8$ deg coincides with the neutral point of the propeller-off condition. It is noted that from a longitudinal stability point of view, only the most forward location of x_{np} is relevant as this will determine the most aft center of gravity location for a given static-margin. For this aircraft, the allowable most aft-location of the center of gravity is therefore driven by the propeller-off condition. However, in practise, the 'propeller-off' condition is a feathered propeller condition, which requires a separate analysis.

Similar to the findings in Ref. [12] for a tip-mounted configuration, the elevator effectiveness increases in a nearly linear fashion with T_C and the slope of the curve depends on the rotation direction. The measured elevator effectiveness is presented in Fig. 14b. At this low angle of attack, the same trend is followed as for ΔC_{m_α}. Although not acquired in this experimental campaign, it is predicted that a high angle of attack, the outboard-up case features a higher $C_{m_{\delta_e}}$ for the same reasons as discussed before. Interestingly, a significant offset can be observed at $T_C = 0$. It is argued that the main contributor to this increased elevator effectiveness comes from the induced upwash to the propeller, resulting in a normal force in the same direction as the load on the horizontal tail. This mechanism is sketched in Fig. 14c and an estimate is given in Fig. 14b for $T_C = 0.18$ for an upwash range of 1 tot 5 degrees.

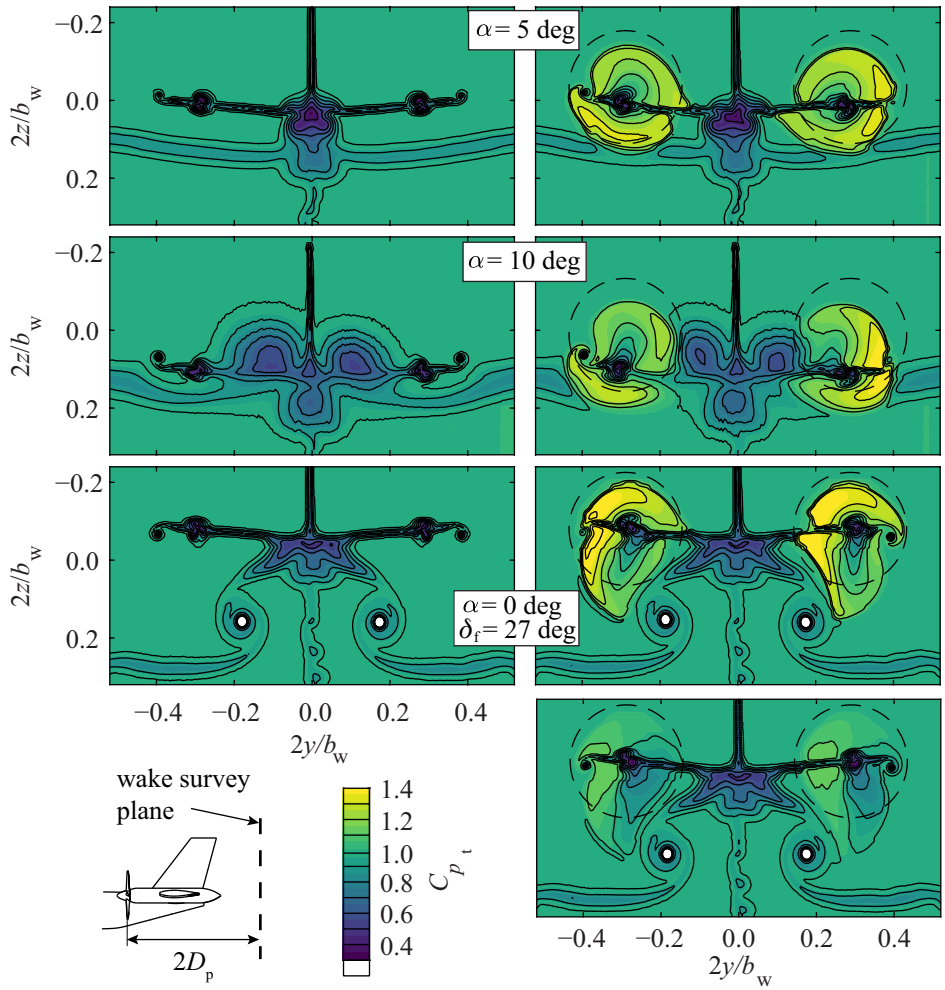

Fig. 13 Measured C_{p_t} behind model for the propeller-off condition (left) and with co-rotating propellers (right). Thrust coefficient T_C = 0.18 for the top three graphs and T_C = 0.01 for the bottom right graph.

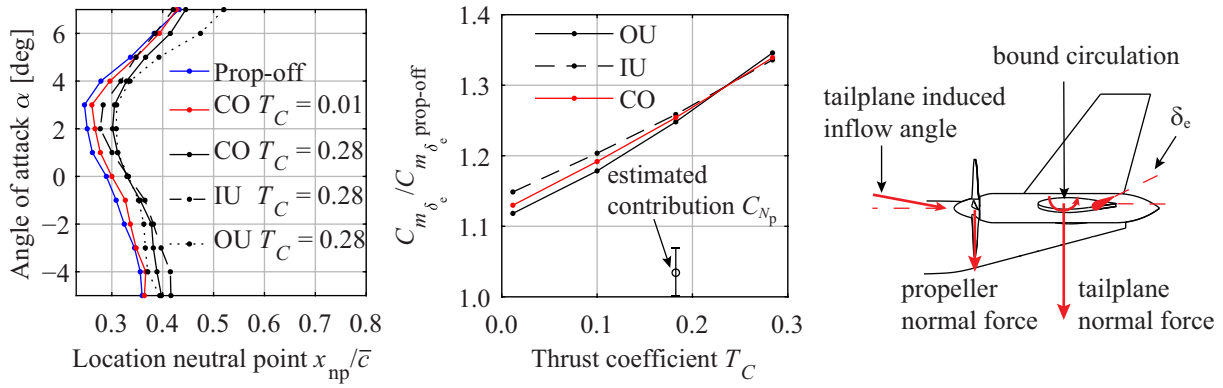

(a) Location of the neutral point based on experimental data.

(b) Measured elevator effectiveness for a deflection δ_e = +15 deg, mean over α =-2 to 2 deg. Estimated effect sketched in (c) with an assumed inflow range of -1 to -5 deg.

(c) Illustration of propeller normal force induced by elevator deflection.

Fig. 14 Effect of propeller installation on location of neutral point and on the elevator effectiveness.

B. Propeller Installation Effects on Directional Stability and Trim

The overall stabilizing contribution of the aft-mounted propellers can also be observed in the yawing moment coefficient, shown in Fig. 15a as a higher C_{n_β}. The change in this slope is a combination of primarily the propeller side force $C_{Y_{p_\beta}}$, the increased contribution of the horizontal tail plane to the directional stability due to its dihedral angle and a modified sideslip angle on the vertical tail by the presence of the propellers. Similarly to the findings in Ref. [8], the for the considered range of conditions, the longitudinal and lateral stability by the propeller installation are not adversely affected. At $\beta = 0$ deg, a non-zero yawing moment exists. This is a combination of the difference in tailplane drag between inboard-up and outboard-up side and a force in y-direction due to the dihedral angle of the tailplane. For a thrust coefficient representative for cruise ($T_C = 0.28$), the combined effect is equivalent to a sideslip angle of $\beta = 0.4$ deg.

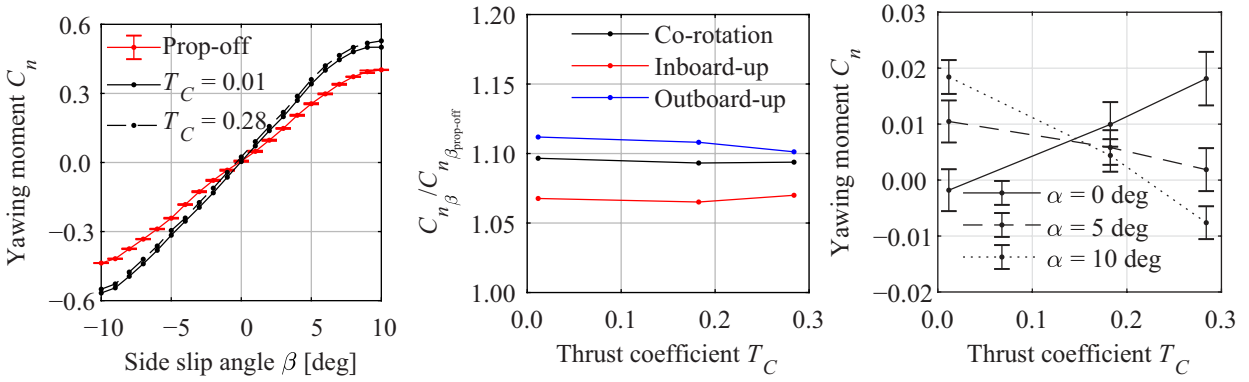

(a) Yawing moment coefficient at $\alpha = 0$ deg.

(b) Evaluated over $\beta = \pm 5$ deg.

(c) Yawing moment as function of thrust coefficient at $\beta = 0$ deg.

Fig. 15 Effect of propeller installation on the aircraft yawing moment coefficient.

When the aircraft experiences a sideslip, the inflow to the propellers is also non-uniform due to the presence of the fuselage, wing and vertical tail. Figure 15b shows a clear dependency of the rotation direction on the C_{n_β} of the aircraft, where the propeller installation, even at a negligible thrust coefficient, enhances the C_{n_β} in the order of 10%. Equivalently to enhanced longitudinal stability due to stabilizing normal force contribution of the propeller, this contribution also increases lateral stability. However, an outboard-up rotation results in a significantly more negative C_{n_β} than the inboard-up case. Although no flowfield data is available, this effect is expected to be the result of a lateral shift in the thrust distribution on the propellers, sketched in Fig. 16 with marked regions on the propeller disk. Because of the chosen z-location, a sideslip leads to a inflowfield to the propeller that results in a higher thrust in regions (1) and (3) and a reduction in region (2) and (4) for the outboard-up case. This lateral shift in thrust yields a yawing moment in the same direction as generated by the vertical tail. The opposite is the case if the propeller is rotating inboard-up, hence the lower contribution to lateral stability. It can be concluded from this section that the extent to which the propeller is contributing to the longitudinal control and stability depends on the angle of attack of the aircraft and the rotation direction of the propellers.

The non-uniformity of the blade loading at angle of attack results in a lateral displacement of the thrust force and to in-plane forces. For co-rotating configuration, both of these phenomenon lead to a yawing moment which is dependent on angle of attack. Table 2 lists the side forces for two angles of attack, which are shown to be in the same direction for both rotation directions. The yawing moment coefficient as a function of thrust coefficient is depicted in Fig. 15c. At $\alpha = 0$ deg, the propeller experiences a net negative angle of attack. Increasing the angle of attack, the regions on the propeller disk with increased thrust shift in y-direction, hence the

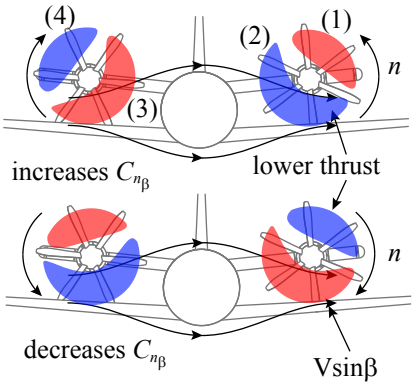

Fig. 16 Schematic of effect sideslip angle on thrust distribution for inboard-up and outboard-up configurations.

change in slope of the curves. For a given offset in y-direction, a higher T_C results in a larger yawing moment, hence the nearly linear trend of the curves. If the yawing moments in Fig. 14c are put into perspective, the maximum values are equivalent to a sideslip angle of 0.5 deg of the propeller-off condition.

Table 2 Installation effect on the time-averaged propeller forces as computed using CFD.

	Outboard-up		Inboard-up	
	α = 0 deg	α = 5 deg	α = 0 deg	α = 5 deg
Thrust $C_T/C_{T_{\text{iso}}}$	0.995	0.995	0.992	0.986
Torque $C_Q/C_{Q_{\text{iso}}}$	0.992	0.981	0.990	0.995
Efficiency $\eta_{\text{p}}/\eta_{\text{p}_{\text{iso}}}$	1.003	1.015	1.001	0.990
Side force $C_Y/C_{T_{\text{iso}}}$	-0.033	-0.126	-0.086	-0.064
Normal force $C_N/C_{T_{\text{iso}}}$	-0.112	0.209	-0.066	0.274

C. Installation Effect on In-Plane and Out-of-Plane Propeller Forces

In this section the non-uniformity of the inflow is further assessed to quantify its effect on the propeller forces. The non-uniformity of the inflow can be expressed as a change in local advance ratio for each section along the propeller blade. To this end, the local change in advance ratio relative to freestream conditions, $\Delta J'$, is determined from the CFD model for the propeller-off condition at the propeller disk and is shown in Fig. 17a.

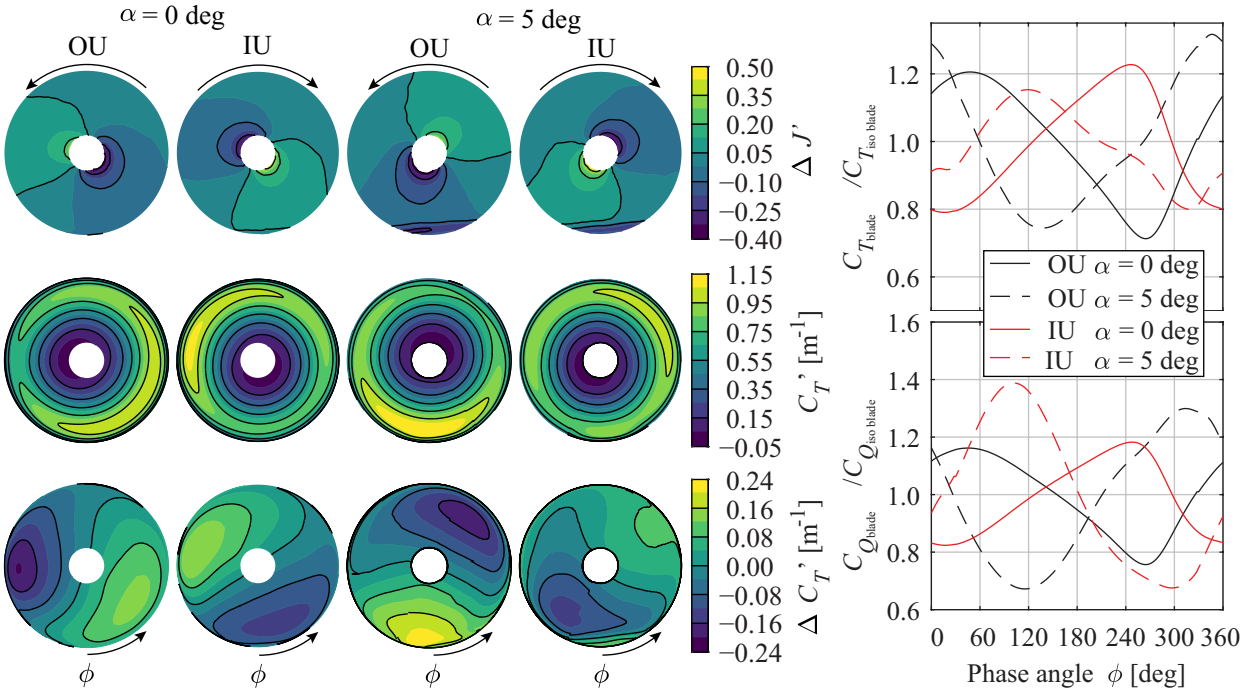

Fig. 17 Propeller thrust distribution and integral blade loads for the installed configuration computed by full blade CFD analyses.

It is noted that this is only an indication of the actual non-uniform inflow field, as the propeller induced pressure field results in a slightly larger inflow to the propeller than a tube with diameter equal to the propeller diameter. At zero angle of attack, the graph shows at phase angle $\phi = 0$ deg that the wing wake just impinges on the blade tips. The asymmetry of the inflow is caused by the wing downwash rather than a change in axial inflow velocity. On average, this leads to a negative angle of attack of the propeller. This is observable as either an increase or decrease in local advance ratio, depending on rotation direction. At $\alpha = 5$ deg, a larger portion of the wing wake impinges the propeller and at the same time the regions of reduced and increased J' have rotated, as the net inflow angle of attack is now positive.

Figure 17a also shows the distribution thrust C'_T, computed by the full-blade CFD simulations, as well as the change in thrust relative to the isolated propeller thrust distribution. It is noted that the absence of windtunnel corrections will slightly affect the mean values, as the isolated propeller thrust is computed in a domain without windtunnel walls. In circumferential direction, the thrust varies as a function of the non-uniformity of the inflow, where the phase angles of higher and lower loading approximately correspond to the phase angles of reduced and increased $\Delta J'$, respectively. As noted in Ref. [18], the outboard regions of the propeller blade are more sensitive to a disturbance than inboard regions. Therefore, the largest changes in load occur around $r/R = 0.8$. The sketched regions of higher and lower dynamic pressure and their dependency on angle of attack in Fig. 12 are clearly traceable to the $\Delta C'_T$ distributions. The thrust force of one blade making a full revolution (Fig. 17b) varies significantly. At $\alpha = 0$ deg the blade thrust and torque fluctuate ±20% around its mean values. It is clear that response to the presence of the wing wake is more pronounced for the outboard-up case at $\alpha = 5$ deg. The locally lower advance ratio for the outboard-up case around $\phi = 0 \pm 30$ deg is further reduced by the wing wake. At these phase angles for the inboard-up case, the majority of the blade experiences a higher advance ratio and only the tip region experiences a reduction in advance ratio. This sharp gradient in non-uniformity is the cause of a relative shallow response to the wake impingement. Despite the rather large fluctuations in blade thrust, the change in integral thrust of the full propeller is negligible, as observed from Table 2.

V. Conclusions

A combined experimental and numerical study was carried out with the objective to quantify the aerodynamic interaction effects between tail-mounted propellers and the airframe of a full aircraft configuration. The understanding of these aerodynamic interactions are important to assess the implication on aircraft stability, control and performance. A representative aircraft geometry was used with nacelles mounted at 69% of span of the horizontal tailplane with either co-rotating, inboard-up or outboard-up rotating propellers. On the same geometry, unsteady RANS CFD computations were performed to quantify the installation effect on component level. In a validation study excellent agreement with the experimental data was found compared. Although the results presented in this paper are for a particular geometry, the qualitative findings can be used for comparable unconventional configurations.

From the balance measurements, it was observed that the propeller installation does not adversely affect the overall stability characteristics of the aircraft compared to the same aircraft in propeller-off conditions, in line with earlier studies. The extent to which the propellers contribute to the longitudinal stability is however highly dependent on propeller rotation direction and the particular location of the propeller on the tailplane. For a constant thrust coefficient, a higher angle of attack results in a more negative moment curve for the outboard-up configuration, while for an inboard-up rotation, the slope approaches the propeller-off condition. For the latter condition, a higher thrust was not found to enhance the longitudinal stability for moderate angles of attack. The installation effect on longitudinal stability for the co-rotating arrangement is found to be the average between the two rotation directions. These findings are contrary to the common observation in existing literature on the wing-tip mounted propeller, where an inboard up rotation results in lower induced losses and a more effective tailplane at positive angles of attack, due to the opposing propeller hub-vortex relative to the tailplane tip-vortex. In this paper, the tip-vortex trailing from the tailplane is in close proximity of the propeller tip-vortex, of which the axial component of vorticity for the inboard-up case has the same sign as the tip-vortex trailing from the tailplane. The location relative to the propeller tip-vortex at which the tailplane tip-vortex is shed, is therefore an important design parameter, and an inboard-up rotation does not guarantee a higher effectiveness of the tailplane if it is not mounted at the tip. In addition to the vortex interaction, at a positive angle of attack, the down-going blade generates a higher dynamic pressure and a higher swirl, with both influence the local normal force gradient on the tailplane. The additional swirl a more dominant factor compared to the increase in dynamic pressure to enhance the local normal force gradient with angle of attack. For an inboard-up rotation, this leads to a lower tailplane effectiveness than to the propeller-off configuration for positive angles of attack. An increase in elevator effectiveness up 40% was found for thrust coefficients representative for cruise conditions. The elevator effectiveness was also found to be enhanced in the zero thrust condition, partially attributed to the propeller normal force as a result

from the tailplane induced upwash, which acts in the same direction as the change in force on the tailplane.

Compared to the isolated propeller, the mean thrust and torque are not significantly altered by the installation. However, the non-uniform inflow to the propeller, driven by changes of in-plane velocities rather than out-of-plane velocity components, creates significant variation in load in circumferential direction. The non-axisymmetric propeller loading leads to a lateral shift in the thrust vector and a yawing moment as function of angle of attack. In combination with differences in tailplane drag between inboard-up and outboard-up, an equivalent sideslip angle of 0.5 deg is found over an angle of attack range of -5 to 14 deg. The extent to which the propeller also enhances lateral stability also depends on propeller rotation direction. The difference in slope of the yawing moment coefficient variation with sideslip between the considered rotation directions is expected to be from the lateral shift in thrust vector due to the non-uniform inflow induced by the fuselage.

The findings of this study provide a deeper understanding of the impact of tail-mounted propellers on the aircraft control and stability, and demonstrates the potential of such configurations as an alternative for future turboprop aircraft.

Acknowledgments

The authors would like to thank Peter den Dulk and Ed Roessen for the manufacturing of the wind-tunnel model. The project leading at these results has received funding from the Clean Sky 2 Joint Undertaking under the European Union's Clean Sky 2 Large Passenger Aircraft program (CS2-LPA-GAM-2014-2015-01).

References

[1] Whitlow, J. B., and Sievers, G. K., "Fuel Savings Potential of the NASA Advanced Turboprop Program," Tech. Rep. TM-83736, NASA, 1984.

[2] Goldsmith, I. M., "A Study to Define the Research and Technology Requirements for Advanced Turbo/Propfan Transport Aircraft," Tech. Rep. CR-166138, NASA, 1981.

[3] Sullivan, W. E., Turnberg, J. E., and Violette, J. A., "Large-Scale Advanced Prop-Fan Blade Design," Tech. Rep. CR-174790, NASA, 1984.

[4] Nicolosi, F., Corcione, S., Della Vecchia, P., Trifari, V., and, Ruocco, M., "Aerodynamic Design and Analysis of an Innovative Regional Turboprop Configuration," *31st Congress of the International Council of the Aeronautical Sciences*, 2018.

[5] Nicolosi, F., Corcione, S., Trifari, V., Cusati, V., Ruocco, R., and Della Vecchia, P., "Performance evaluation and DOC Estimation of an Innovative Turboprop Configuration," *AIAA Aviation Forum*, 2018. doi:10.2514/6.2018-3662.

[6] Hoogreef, M., Vos, R., de Vries, R. and Veldhuis, L. L. M., "Conceptual Assessment of Hybrid Electric Aircraft with Distributed Propulsion and Boosted Turbofans," *AIAA Science and Technology Forum and Exposition*, 2019. doi:10.2514/6.2019-1807.

[7] Hoogreef, M. and Vos, R., "System-level assessment of tail-mounted propellers for regional aircraft," *ICAS 2018: 31st Congress of the International Council of the Aeronautical Sciences*, 2018.

[8] Applin, Z. T., and Coe, P. L., Jr, "Low-Speed Stability and Control Characteristics of a Transport Model with Aft-Fuselage-Mounted Advanced Turboprops," Tech. Rep. NT-2535, NASA, 1986.

[9] Ridder, S.-O., "Wind Tunnel of a Twin, Rear Propeller Transport Aircraft Configuration at Low Speeds," *14th ICAS Congress*, Vol. 2, 1984, pp. 644–654.

[10] de Young, J., "Propellers at high incidence," *Journal of Aircraft*, Vol. 23, No. 3, 1965, pp. 241–250. doi:10.2514/3.43646.

[11] Ortun, B., Boisard, R., and Gonzalez-Martino, I., "In-plane airloads of a propeller with inflow angle: prediction vs. experiment," *30th Applied Aerodynamics Conference*, 2012. doi:10.2514/6.2012-2778.

[12] van Arnhem, N., Sinnige, T., Stokkermans, T. C. A., Eitelberg, G., and Veldhuis, L. L. M., "Aerodynamic Interaction Effects of Tip-Mounted Propellers Installed on the Horizontal Tailplane," *AIAA Aerospace Sciences Meeting*, 2018. doi: 10.2514/6.2018-0542.

[13] Sinnige, T., van Arnhem, N., Stokkermans, T. C. A., Eitelberg, G., and Veldhuis L. L. M., "Aerodynamic Analysis of a Wingtip-Mounted Tractor-Propeller Configuration," *Journal of Aircraft*, Vol. 56, No. 1, 2018, pp. 295–312. doi:10.2514/1.C034978.

[14] Veldhuis, L.L.M., "Propeller Wing Aerodynamic Interference," Ph.D. Thesis, Delft University of Technology, Delft, The Netherlands, 2005.

[15] Tenerowicz, T., "Flow Behind Single-and Dual-Rotation Propellers at Angle of Attack," *23rd Joint Propulsion Conference*, 1987. doi:10.2514/6.1987-1750.

[16] Sinnige, T., de Vries, R., Della Corte, B., Avallone, F., Ragni, D., Eitelberg, G., and Veldhuis, L. L. M., "Unsteady Pylon Loading Caused by Propeller-Slipstream Impingement for Tip-Mounted Propellers," *Journal of Aircraft*, Vol. 55, No. 4, 2018, pp. 1605–1618. doi:10.2514/1.C034696.

[17] Li, Q., Öztürk, K., Sinnige, T., Ragni, D., Eitelberg, G., Veldhuis L. L. M., and Wang, Y., "Design and Experimental Validation of Swirl-Recovery Vanes for Propeller Propulsion Systems," *AIAA Journal*, Vol. 56, No. 12, 2018, pp. 4719–4729. doi:10.2514/1.J057113.

[18] van Arnhem, N., Vos, R., and Veldhuis, L. L. M., "Aerodynamic Loads on an Aft-Mounted Propeller Induced by the Wing," *AIAA Aerospace Sciences Meeting*, 2019. doi:10.2514/6.2019-1093.

[19] Bass, R. M., "Small Scale Wind Tunnel Testing of Model Propellers," *AIAA 24th Aerospace Sciences Meeting*, 1986. doi: 10.2514/6.1986-392.

[20] ANSYS® Academic Research Release 18.1, "Help System, Fluent," ANSYS, Inc.

[21] Stokkermans, T. C. A., van Arnhem, N., Sinnige, T. and Veldhuis, L. L. M., "Effects of wingtip-mounted propellers on wing lift and induced drag," *AIAA Journal*, Vol. 57, No. 2, 2019, pp. 566–580. doi:10.2514/1.J057398.

[22] Spalart, P. R., and Rumsey, C. L., "Effective Inflow Conditions for Turbulence Models in Aerodynamic Calculations," *AIAA Journal*, Vol. 45, No. 10, 2007, pp. 2544–2553. doi:10.2514/1.29373.

[23] Durand, W., *Aerodynamic Theory Vol. IV.*, Julius Springer, 1935.